ORIGINAL ARTICLE

Straw-derived biochar as the potential adsorbent for U(VI) and Th(IV) removal in aqueous solutions

Qingzhou Zhao[1,2,3] · Zhihong Xu[1] · Zhisheng Yu[2]

Abstract

The radioactive uranyl and thorium ions discharged into freshwater have been the imperative environmental issue arousing great concern. Biochar, owing to its low cost, operational ease, and high efficiency, is touted as the promising sorbent for the U(VI) and Th(IV) removal in aqueous solutions. This study employed several characterization techniques and batch experiments to investigate mechanisms of U(VI) and Th(IV) adsorption on biochar. The kinetic results exhibited the fitness of the pseudo-second-order model. Both U(VI) and Th(IV) removals were influenced by pH, while only the ionic strength effects on U(VI) adsorption were observed. The adsorption of either the U(VI) or the Th(IV) fitted to the Langmuir and Freundlich model well. Natures such as endothermicity, increasing randomness, feasibility, spontaneity, and temperature favor of the adsorption reaction could be found in U(VI) and Th(IV) adsorption (U: $\Delta H_0 = 36.28$, $\Delta S_0 = 108.84$ and $\Delta G_0 < 0$; Th: $\Delta H_0 = 63.42$, $\Delta S_0 = 134.12$ and $\Delta G_0 < 0$). Our results highlighted the importance of biochar as the potentially green adsorbent and provided a practical strategy for radioactive contaminant remediation.

1 Introduction

With the rapid development of the nuclear power industry, the radioelement contaminants discharged into freshwater have aroused great concern due to their toxicity and carcinogenicity to human health [1–4]. The risks of radionuclide wastes stored for the long-term depend on their fate and transport in the geosphere [2, 5]. The mobility of common radionuclides such as Uranium and Thorium is always depicted by the adsorption of aqueous U(VI) and Th(IV) exposed in the environment respectively [2, 6]. Adsorptions of the U(VI) and Th(IV) radioelements are regarded as promising approaches to limit the dispersal of radionuclide pollution in the hydrosphere and pedosphere [7–9]. The interactions between these radionuclides and their potential adsorbents remained to be investigated [10–18]. Thus, the discovery of a low-cost, highly effective, and easy-to-operate adsorbent material is considered the key barrier for the development of radionuclide contaminant remediation and nuclear waste disposal.

Biochar, as the emerging green material, is placed great expectation of the promising prevalent adsorbent for U(VI) and Th(IV) removal. Biochar is the carbonaceous residue derived from a pyrogenic process using carbon-rich biomass as the feedstocks in an oxygen-limited environment [19–23]. Biochar is ubiquitous in the ecosphere and interconnects with numerous contaminants. It could regulate the transport, fate, and bioavailability of contaminants in the environment [21, 22, 24–26]. The adsorption of positive ions such as heavy metals or rare earth elements is found on the negative surface of biochar with electronic attractions [15, 19, 25, 27–30]. These contaminants could also be transformed into composites and precipitates due to the ligands and functional groups on the biochar surface [31–33]. Similar parameters such as high micro-porosity, surface heterogeneity, and superficial area are found on

✉ Zhisheng Yu
yuzs@ucas.ac.cn

1. Centre for Planetary Health and Food Security, Griffith University, Nathan, QLD 4111, Australia

2. College of Resources and Environment, University of Chinese Academy of Sciences, 19 A Yuquan Road, Shijingshan District, Beijing 100049, People's Republic of China

3. College of Urban and Environmental Science, Peking University, 5 Yiheyuan Road, Beijing 100871, People's Republic of China

biochar and activated carbon, which is the most prevalent carbonaceous sorbent prepared by pyrolysis as well [34, 35]. Nevertheless, biochar could be amended as the adsorbent directly without the thermal or chemical modification on its surface like activated carbon [31, 34, 36]. This optional ease is attributed to the various physical, chemical, and mechanical characteristics of biochar originating from the diversification of preparing conditions such as feedstock type, pyrolysis temperature, and retention time. These features made biochar acquire flexibility for extensive applicability of environmental remediation through optimizing it into the most efficacious properties. Only a few studies have paid attention to the adsorption capacity of radionuclides using this economical and effective sorbent biochar. Biochar with the modification of potassium permanganate, polyethyleneimine, and ferriferous oxide was employed for the radionuclide removal [37–39]. However, most of these sorbents took the bacteria biomass and aerial root rather than the easily available biowaste as the feedstock. Especially, the practice of the direct amendment of biochar for U(VI) and Th(IV) without any modification removal is urgently needed to utilize the optional ease and low-cost trait of biochar. In addition, although the co-occurrence of U(VI) and Th(IV) is prevalent, knowledge about the comparison between the adsorption of them remains unknown. Hence, it is essential to understand the processes mechanism of aqueous U(VI) and Th(IV) elimination using the raw biochar derived from easily available straw.

This study aims to investigate the capacity and mechanism of biochar adsorption for U(VI) and Th(IV) and the discrepancy between these sorption processes. To achieve these objectives, biochar derived from straw was characterized by SEM, EDS, TEM, XPS, FTIR, and Raman spectra respectively. Adsorption processes with the various contact time, temperatures, and pH were carried in batch mode to clarify the kinetics, thermodynamic, and mechanism of the U(VI) and Th(IV) elimination.

2 Method and material

2.1 Biochar preparation

The biochar was originated from straws of wheat (*Triticum aestivum*) as the feedstock. The air-dried wheat straws were put in a stove at 60 ℃ for 24 h. All the biochar was produced by pyrolysis through thermal decomposition with the oxygen-insulated condition. The temperature is 400 ℃ and the retention time is 2 h respectively. The pyrolysis process was performed in a custom-made stainless-steel furnace. The derived biochar particles were sieved with 0.2-mm sieves for the subsequent characterizations and batch experiments.

2.2 Biochar characterization

The morphological images were obtained using a scanning electron microscope (SEM, 15 JSM-6360LV) and a transmission electron microscope (TEM, JEM-1011). Fourier transform infrared spectroscopy (FTIR, Thermo Nicolet, 8700, Madison, WI, USA) with the scan range of 4000–400 cm^{-1} and Raman spectra (Mettler Toledo, Zurich, Switzerland) were employed to determine the functional groups on the biochar surface. Taking the monochromatized Al K alpha X-ray (hm = 1486.6 eV) as the radiation source, an element analysis was carried out by using the X-ray photoelectron spectroscope (XPS, Thermo ESCALAB250 analyzer) at a constant pass energy of 20 eV. After the calibrated binding energies of the photoelectrons, C 1 s and O 1 s peak occurred at 284.6 eV and 532.7 eV respectively. The specific surface area of the biochar was recorded based on the Brunauer–Emmett–Teller (BET) adsorption/desorption curves in the nitrogen atmosphere to verify the porosity of the biochar [40].

2.3 Batch experiment

The batch experiments for the analogue processes of biochar adsorption processes to eliminate the aqueous Uranium and Thorium radionuclides were conducted in polyethylene centrifuge tubes. No attempt was applied to regulate the ambient air condition among all the treatments. Various treatments with the variant contact time, initial concentration, pH, ion strength, and temperature were conducted to investigate their influence on biochar adsorption for U(VI) and Th(IV) removal. NaNO$_3$ solution mixed with biochar was prepared for pre-equilibrium as the background electrolyte. The desired initial concentration of analogue contaminant was obtained by adding the U(VI) and Th(IV) stock solutions into the biochar electrolyte suspension. Then, to achieve the target pH value in a suitable range for U(VI) and Th(IV) adsorption, a NaOH or HCl solution was added with a negligible volume of 0.01 and 0.1 mol/L. Biochar particles were added into the radionuclide solutions to obtain the suspensions with the solid-to-liquid ratio of 0.5 g/L. Shaking of the polyethylene test tubes was performed in an end-over-end tumbler to reach the adsorption equilibrium. The test tubes were shaken with the conditions of various times (10, 20, 30, 40, 50, 60, 70, 80, 90, 100, 110, and 120 min), and the temperature (293 K, 313 K, and 333 K) to clarify the kinetics and isotherms. The kinetic investigation also took 10, 25, 50, and 70 g/mL as the initial concentration of radionuclide ion when the pH value was 5.0 and the temperature was 293 K. After separating the liquid and solid phase of the

suspension with centrifugation at 9000 rpm for 40 min, the U(VI) and Th(IV) concentrations were measured using a spectrophotometry tool. Taking the U(VI) and Th(IV) loss on the centrifuge tube wall into the consideration, identical control treatments without biochar were also carried out separately to obtain the calibration curves. The adsorbed mass of U(VI) and Th(IV) was subsequently computed according to the deduction of the solution mass from the mass spike. The concentrations of U(VI) and Th(IV) were measured by using a UV–vis spectrophotometer at 652 nm and 660 nm respectively [41, 42]. The sorption-related parameters were calculated as the following equations:

$$\text{sorption percentage} = (C_0 - C_e)/C_0 \times 100 \qquad (1)$$

C_0 represents the initial metal concentration (g/L). C_e indicates the metal concentration at equilibrium (g/L). All the experimental data were collected based on the average of the triplicate by repeated measurements. The fractional errors of the data were limited to 5%.

3 Results and discussion

The straw-derived biochar was employed for radionuclide removal through adsorption processes. The biochar prepared from straw pyrolysis consisted of irregular stacks with the deposition of stable aromatic rings [21, 43] (Fig. 1). The biochar surface shaped favorable environments for the formation of functional groups such as carbonyl, carboxyl, and hydroxyl groups. These alkaline or oxygen-containing functional groups provided the potential of biochar as the promising adsorbent for the U(VI) and Th(IV) contaminants in aqueous solutions [21, 44]. The unstable surface of sorbent might also combine with nuclide ions to form the precipitation. In this study, the solid phase was removed from the suspension employing biochar as the adsorbent by the

Fig. 1 Biochar preparation and U(VI) and Th(IV) adsorption mechanism on biochar

filtration. Both the nuclide contaminants either combined on the biochar surface or were taken into the precipitation with separation from the radionuclide solutions after the adsorption processes.

3.1 Characterization

3.1.1 SEM, TEM, and EDS

The SEM and TEM images of the biochar before and after the U(VI) and Th(IV) uptake were obtained to reflect the biochar structure explicitly. Figure 2 shows the porous structure and opening shape of biochar, which were the vital characteristics for the aqueous adsorption. The permeable structure with plenty of intra-pores made biochar continuously combine with U(VI) and Th(IV) ions after the functional groups on the biochar surface were occupied. The raw biochar without radionuclide adsorption possessed smooth pore walls on the internal and external surfaces. After U(VI) and Th(IV) adsorption reached equilibrium, the biochar surface and the intra-pores became coarse and bumpy. This roughness might be caused by the coating of the radionuclide ions and corrosion of the biochar [30]. The EDS spectrum after U(VI) and Th(IV) adsorption demonstrated new peaks of U(VI) and Th(IV) respectively, which were not found on the raw biochar (Fig. S1 & Fig. S2). These results pointed out that the adsorptions were attributed to ion exchange, and bindings on biochar surface might explain the main form of the aqueous radionuclide removal.

3.1.2 FTIR and Raman spectrum analysis

Figure 3 depicts the FTIR and Raman spectra of biochar before or after the radionuclide adsorption to characterize the functional groups on the surface of biochar. The FTIR data of raw biochar and biochar after U(VI) and Th(IV) removal in the wave region of 500–4000 cm^{-1} are presented in Fig. 3A. The FTIR results indicated the presence of functional groups on biochar surfaces such as O–H, C-H, C-O, and C–C to engage in the U(VI) and Th(IV) adsorption. The broadest peaks occurred at 1095.57 cm^{-1}, which could be assigned to the strong C-O vibration representing two hydroxyl groups; the peaks at 1430.35 and 796.30 cm^{-1} were regarded as C-H bending vibrations related to aliphatic and aromatic hydrocarbon and alkene; peaks at 465.64 cm^{-1} exhibited the presence of C–C skeleton vibration corresponding to hydrocarbon from phenol and branched alkanes; at 3318.57 cm^{-1}, peaks representing the O–H stretching vibration attributed to hydroxyl groups in ethanol or phenol could be found [30, 45]. After U(VI) and Th(IV) adsorption, an obvious increase in the intensities of
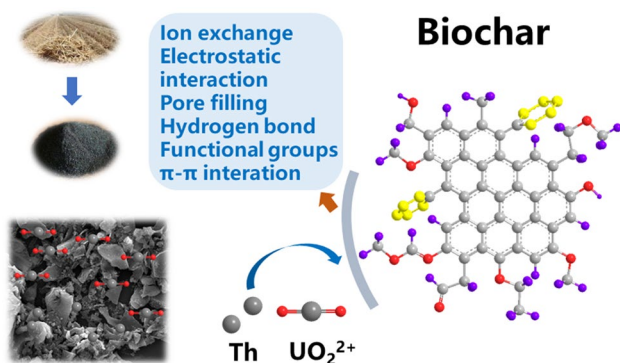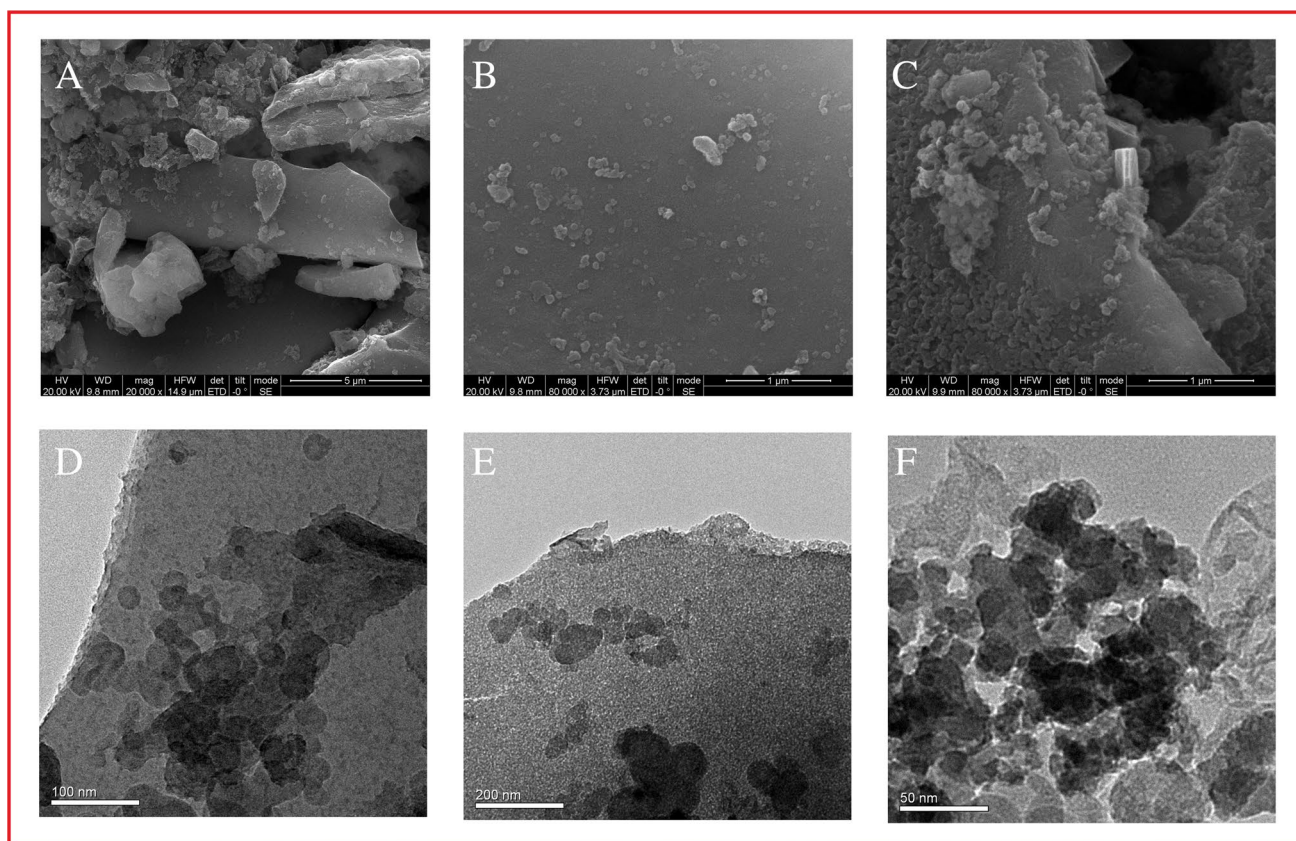
Fig. 2 Scanning electron microscope (SEM) images of the raw biochar (**A**), the biochar after U(VI) adsorption (**B**) and the biochar after Th(IV) adsorption (**C**). Transmission electron microscope (TEM) of the raw biochar (**D**), the biochar after U(VI) adsorption (**E**), and the biochar after Th(IV) adsorption (**F**)
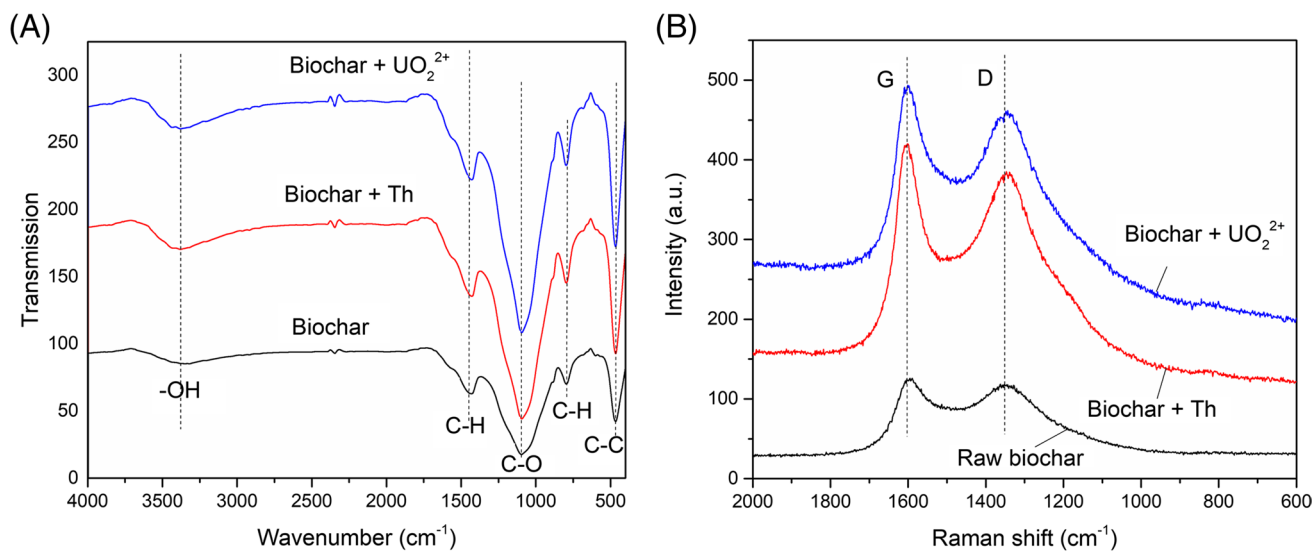

Fig. 3 FTIR (**A**) and Raman (**B**) spectra of biochar before and after U(VI) and Th(IV) adsorption

all these peaks could be observed compared to that of the raw biochar. This finding revealed the depth participation of these functional groups in the radionuclide adsorption reactions. Figure 3B shows the Raman spectra results of biochar before or after the U(VI) and Th(IV) adsorption in the wavelength region of 600–2000 cm^{-1}. After the radionuclide removal processes, a significant change of G bands could be observed to prove the engagement of sp^2 carbon atoms in the adsorption. sp^2 carbon could be attributed to π electron interaction mechanisms and demonstrated the double bonds and graphitic nature of biochar. Meanwhile, the D band intensity varied before or after the U(VI) and Th(IV) adsorption. Correspondingly, the D/G ratio also altered with the adsorption processed. These changes were imputed to the breathing modes of disordered graphite rings on the biochar surface [46, 47].

3.1.3 XPS analysis

Figure 4 exhibits the XPS spectra of C1s and O1s groups on the biochar surface before and after the radionuclide adsorption. The broadest peaks representing C–C (sp^2-carbon) and C–C (sp^3-carbon) were classified at the binding energy of 284.4 eV and 284.8 eV (Fig. 4A). After U(VI) and Th(IV) adsorption, only the peaks of C–C

(sp^3-carbon) were observed at 284.8 eV, and these peaks showed an increase of intensity compared to raw biochar (raw biochar: 42.56%, biochar + U: 57.43%, biochar + Th: 47.15%) (Fig. 4B & C). Peaks corresponding to carbonyl groups C–O–C showed acute elevation after U(VI) and Th(IV) adsorption processes (raw biochar: 5.94%, biochar + U: 36.90%, biochar + Th: 38.25%). The peak at 285.4 eV representing C-O groups decreased significantly after U(VI) adsorption, while it remained similar proportion with raw biochar (raw biochar: 18.06%, biochar + U: 5.68%, biochar + Th: 14.59%) [30, 48]. With respect to the O1s XPS spectra, the broadest peaks at 531.5 eV could be ascribed to carbonyl C = O stretching vibration, which indicated the presence of the carbonyl, ketone, lactone, and quinine groups. These C = O groups decreased significantly after U(VI) and Th(IV) adsorption (raw biochar: 39.51%, biochar + U: 21.92%, biochar + Th: 22.50%). However, the relative percentage of the carboxylic C-O = C increased after the radionuclide removal (raw biochar: 45.16%, biochar + U: 60.85%, biochar + Th: 55.20%). The peak elevation was also observed at 533.5 eV, which indicated the increase of the carbonyl bond C-O (raw biochar: 15.33%, biochar + U: 17.23%, biochar + Th: 22.24%) (Fig. 4) [15, 49]. These findings revealed that the U(VI) and Th(IV) adsorption was completed through the redox
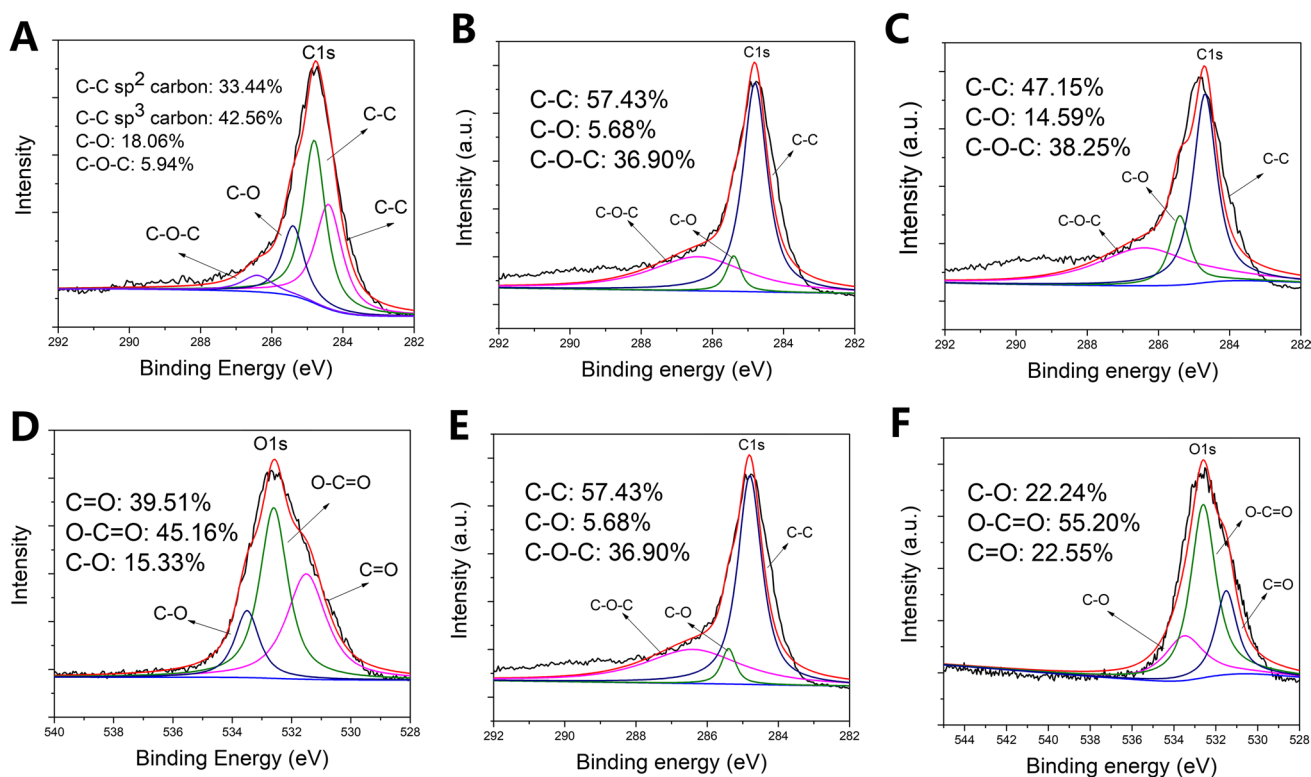

Fig. 4 High-resolution X-ray photoelectron spectroscopy (XPS) spectra of C1s before (**A**) and after U(VI) and Th(IV) reaction (**B**, **C**) and O1s before (**D**) and after U(VI) and Th(IV) adsorption (**E**, **F**)

chemical reaction with various carbonic and oxygenated groups on the complex surface of biochar.

3.1.4 BET analysis

To monitor the porosity characteristic of the sorbent, Brunauer–Emmett–Teller (BET) adsorption/desorption curves were employed in the nitrogen atmosphere to calculate the specific surface area of the biochar. This study recorded an S_{BET} value of 25.666 m^2/g according to the biochar pyrolyzed with 400 °C for 2 h, which was obviously lower than the previously reported biochar derived from other straws as the feedstocks under the condition of 600 °C and 3 h [2]. Notably, the S_{BET} of biochar pyrolyzed from poplar shaving wood with 600 °C for 3 h did not distinguish from the biochar employed in this study. Lignin possessed higher contents of phenolic and aromatic carbons than cellulose to produce stiff bonds among cross-links. The molecular flexibility decreased, and the decomposition temperature was elevated by these stiff bonds during the pyrolysis [50, 51]. Therefore, the straw-derived biochar with higher cellulose percentage was more sensitive to the pyrolysis temperature and retention time than the wood-derived biochar with higher lignin percentage [40].
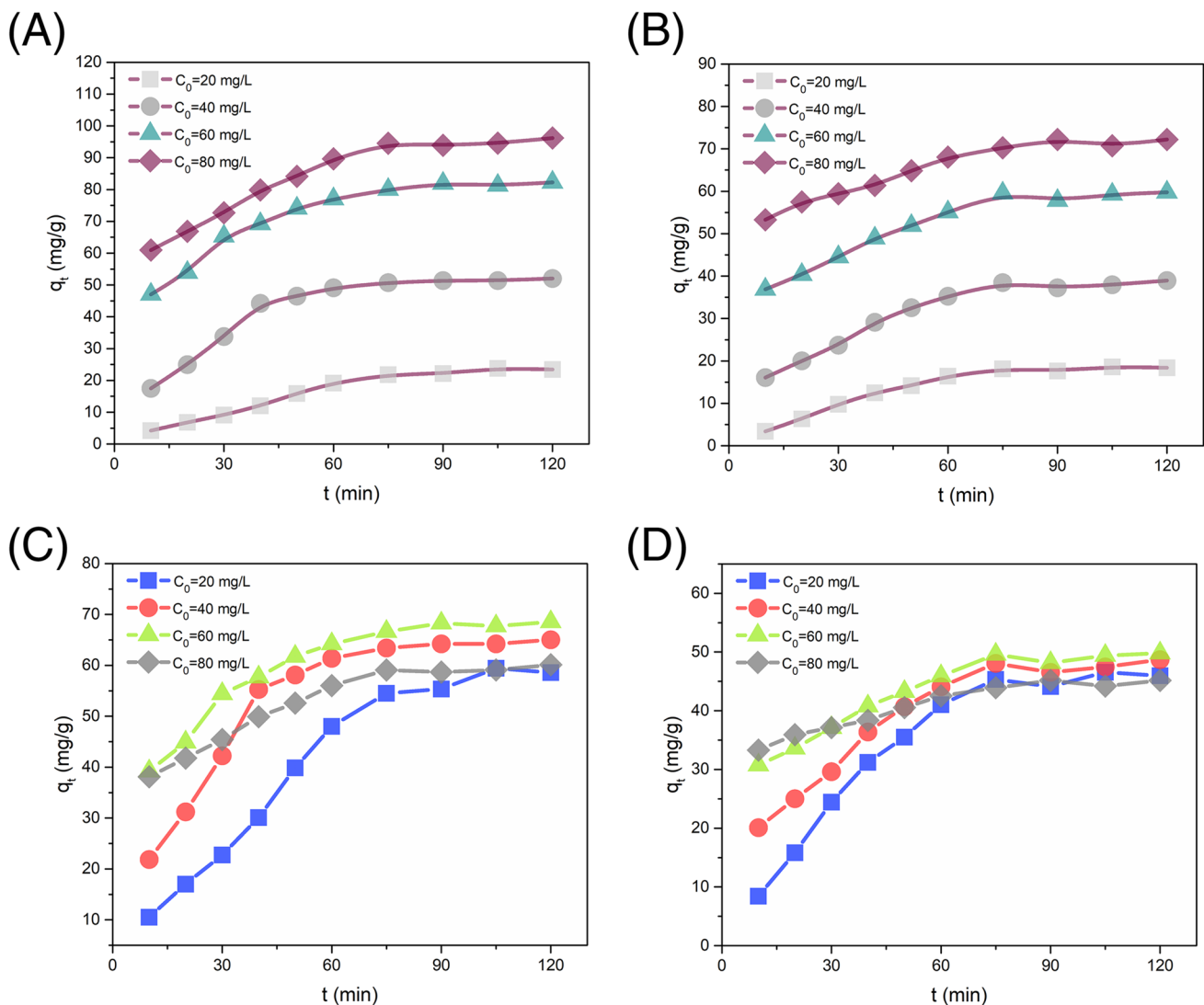

Fig. 5 Adsorption capacity and percentage of U(VI) (**A**, **C**) and Th(IV) (**B**, **D**) on biochar as a function of contact time. Adsorption capacity indicates the removed amounts of the contaminants when the adsorption process reached the equilibrium. Adsorption percentage indicates the removed percentages of the contaminants when the adsorption process reached the equilibrium

3.2 Adsorption kinetics

To investigate the kinetics of the U(VI) and Th(IV) removal, the adsorptions on the biochar were determined as the contact time went by (Fig. 5). Results demonstrated the acute rise of adsorption quantities for both U(VI) and Th(IV) sequestration in the initial 75 min. These trends displayed the highly efficient sorption mainly derived by the abundant functional groups on the biochar surface in the initial time. Subsequently, the increasing curve was flattened and adsorption was maintained at a high level. This indicated that the functional groups on the biochar surface were gradually occupied so that the adsorption processes reached equilibrium. Simultaneously, the adsorption quantities of the radionuclide always increased with the increasing initial pollutant concentration. The kinetics of adsorption percentage for U(VI) and Th(IV) showed a similar tendency to adsorption capacity. A certain amount of initial contaminant was essential to provide the driving force to overcome all mass transfer resistance of radionuclides between the aqueous and solid phases for completing the maximum adsorption [52, 53]. Notably, the radionuclide removal with the initial U(VI) and Th(IV) concentration of 60 mg/g reached the maximum adsorption percentage. When the initial Uranium and Thorium concentration exceeded the optimal value, energetically less favorable sites become involved owing to the saturation of the biochar surface. The interaction between radionuclide ions and biochar was also weakened because of the lower mobility of ions compared to the diluted solution [42, 54]. For these observations, the straw-derived

biochar showed superior capacity and reached equilibrium with the retention of U(VI) and Th(IV) after 75 min. The straw-derived biochar showed superior capacity in U(VI) and Th(IV) adsorption process compared to the previously used sorbents (Table S1).

Two prevalent kinetics models, pseudo-first-order kinetic model and pseudo-second-order kinetic model, which were popularly used to clarify the mechanism of the granular ion adsorption process in aqueous solution, were employed in these biochar sorptions (Tan et al. 2014). The two prevalent kinetic models pseudo-first-order kinetic model and pseudo-second-order kinetic model were generally expressed below respectively:

$$\ln\left(q_e - q_t\right) = \ln q_e - k_1 t \tag{2}$$

$$\frac{t}{q_t} = \frac{1}{k_2 q_e^2} + \frac{t}{q_e} \tag{3}$$

Both U(VI) and Th(IV) adsorption fitted better to the pseudo-second-order kinetic model than to the pseudo-first-order kinetic model (Table S2). This finding was consistent with the previous study about radionuclide adsorption in aqueous solutions [4, 16, 55]. After the adsorption processes, contaminant ions were heterogeneously distributed on the biochar surface. The electrons sharing and exchanging adsorbate and adsorbent accompanying valence forces in the chemical sorption and chemisorption on the biochar surface might explain this phenomenon. The elimination of U(VI) and Th(IV) and the complexation between the radionuclides and functional groups were also observed on the biochar surface [28, 56–60].
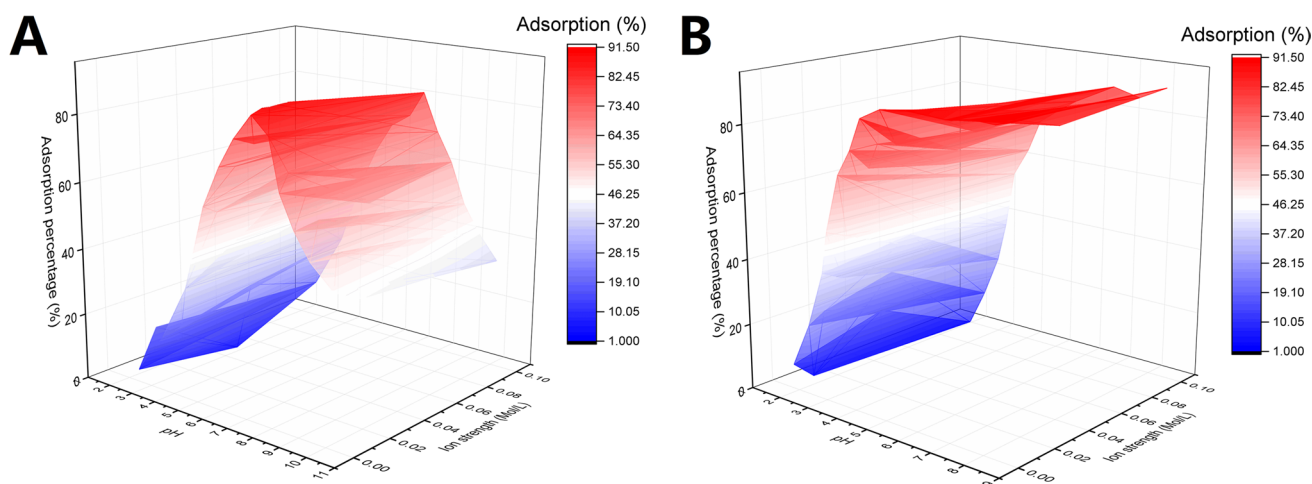

Fig. 6 Effect of pH and foreign ions on U(VI) (**A**) and Th(IV) (**B**) adsorption on biochar

3.3 Effect of pH and ionic strength

Another two factors, pH and ionic strength, which were important to optimize the adsorption process, were employed for the assessment of their influence on the U(VI) and Th(IV) removal capacity. The results depicted that the U(VI) adsorption percentage grew drastically with a pH value in the range of 2.0–7.0, while the reverse tendency occurred in the pH range of 7.0–11.0 (Fig. 6A). As for the Th(IV) removal, the adsorption percentage grew with the pH from 2.0 to 4.0, and a steep increase could be observed near pH = 4.0. Then, the curve was flattened and maintained at the same level in the pH range of 4.0–9.0 (Fig. 6B). The increasing tendency of adsorption percentage at a very low pH range might be mainly attributed to the functional groups such as carboxylate and hydroxyl on the biochar surface. The biochar surface became positively charged since these groups were protonated in the proton-rich acidic solution. The radionuclide cations were therefore electrostatically repulsed by the positively charged biochar surface. When the pH value increased, the electrostatic repulsion changed to electrostatic interaction. For instance, in strongly acidic solutions, Uranium was mainly presented in the form of divalent uranyl ion UO_2^{2+} [13]. Under the weak acidic condition, the dominant forms of U(VI) came into $UO_2(OH)^+$, $(UO_2)_2(OH)_2^{2+}$ dimer, and $(UO_2)_3(OH)_5^{2+}$ trimer through the hydrolysis of UO_2^{2+} ions. The electrostatic interaction between these positive ions and negatively charged biochar surfaces facilitated the U(VI) adsorption [61, 62]. Apart from this electrostatic effect, the aqueous cation such as H^+ and H_3O^+ might compete for the available sorption sites on the biochar surface with the radionuclide cations. As the pH value of the aqueous solution increased, more binding sites were released and the cation competition was consequently eliminated. Moreover, the deprotonation of functional groups also alleviated the proton formed in the acidic solutions, and the radionuclide ions converted to anion forms again [63]. The steep increase of Th(IV) adsorption near pH 4.0 is a case in point for these deprotonation effects. This result was owed to the deprotonation of the carboxylic moieties on the biochar surface. The proceeding Th(IV) hydrolysis and polynucleation brought about the $Th(OH)_4$ precipitation eventually [4, 64]. Referring to the reduction of U(VI) adsorption percentage in the pH range of 7.0–11.0, it coincided with the previous results indicating that the aqueous adsorption might be impaired through the formation of hydroxide complexes. Thus, the optimal pH values of U(VI) and Th(IV) removal capacity were 7.0 and 11.0 respectively.

On the other hand, Fig. 6 also exhibits the ionic strength effect on the radionuclide removal. There is no strong correlation between Th(IV) adsorption capacity and ionic strength. This independence of the adsorption to the background ionic strength might imply the inner-sphere surface complexation of the adsorption [62]. This finding was also supported by previous studies about radionuclide adsorption [41, 63, 65, 66]. The U(VI) adsorption capacity increased with the presence of the interfering ion Na^+ in the pH range of 2.0–7.0, yet the U(VI) adsorption capacity showed a negative correlation with Na^+ ion in the pH range of 7.0–11.0. The aforementioned deprotonation effect and cation competition might be accountable for this result [63]. In the acidic environment, the Na^+ cation competed for the binding site with the Uranium cation on the biochar surface. When the solution became alkalic, the Uranium was deprotonated to an anion and no longer competed with Na^+ ions.

3.4 Adsorption isotherms studies

Figure 7 presents the adsorption isotherms of U(VI) and Th(IV) at various temperatures of 293 K, 313 K, and 333 K for better understanding. Both the U(VI) and Th(IV) adsorption quantities ascended with the rising temperature. This finding showed the high-temperature preference of both two radionuclide adsorption processes on biochar. To further study the mechanism and quantization of U(VI) and Th(IV) removal, two prevalent empirical models, Langmuir and Freundlich models, were employed to fit the data of these aqueous radionuclide removal experiments (Tan et al. 2015). The linear form of the Langmuir equation could be expressed as $\frac{1}{q_e} = \frac{1}{q_{max}} + \frac{1}{bq_{max}}\frac{1}{C_e}$. q_{max} (mg/g) represents the maximum loading quantity of the U(VI) and Th(IV) adsorbate per unit weight of biochar; q_e (mg/g) is the radionuclide amount of unit weight of biochar at equilibrium concentration; b (L/mg) indicates the Langmuir constants depending on adsorptive energy; and C_e represents the equilibrium concentration of U(VI) and Th(IV) anions (mg/g) [19]. Freundlich model could be described as $q_e = K_F C_e^n$ or the modified linear form: $\log q_e = \log K_F + n \log C_e$. K_F (($mg^{1-n} \cdot L^n$)/g) indicates the Freundlich constant interrelated to the adsorption capacity; n represents the dependent degree in adsorptive contaminant sorption process at the equilibrium concentration [67]. Either Langmuir or Freundlich model gave a great fit to both the U(VI) and Th(IV) removal processes (Table 1). The Langmuir model is appropriate for the sorption process on the monolayer surface, while the Freundlich model is always applied for the adsorption on the multi-layer surface rather than on the restricted monolayer [10, 19, 68–72]. Since biochar was prepared with the uncertain pyrolysis condition, the corresponding various properties and structures made its partial surface both homogeneous and heterogenous [73].
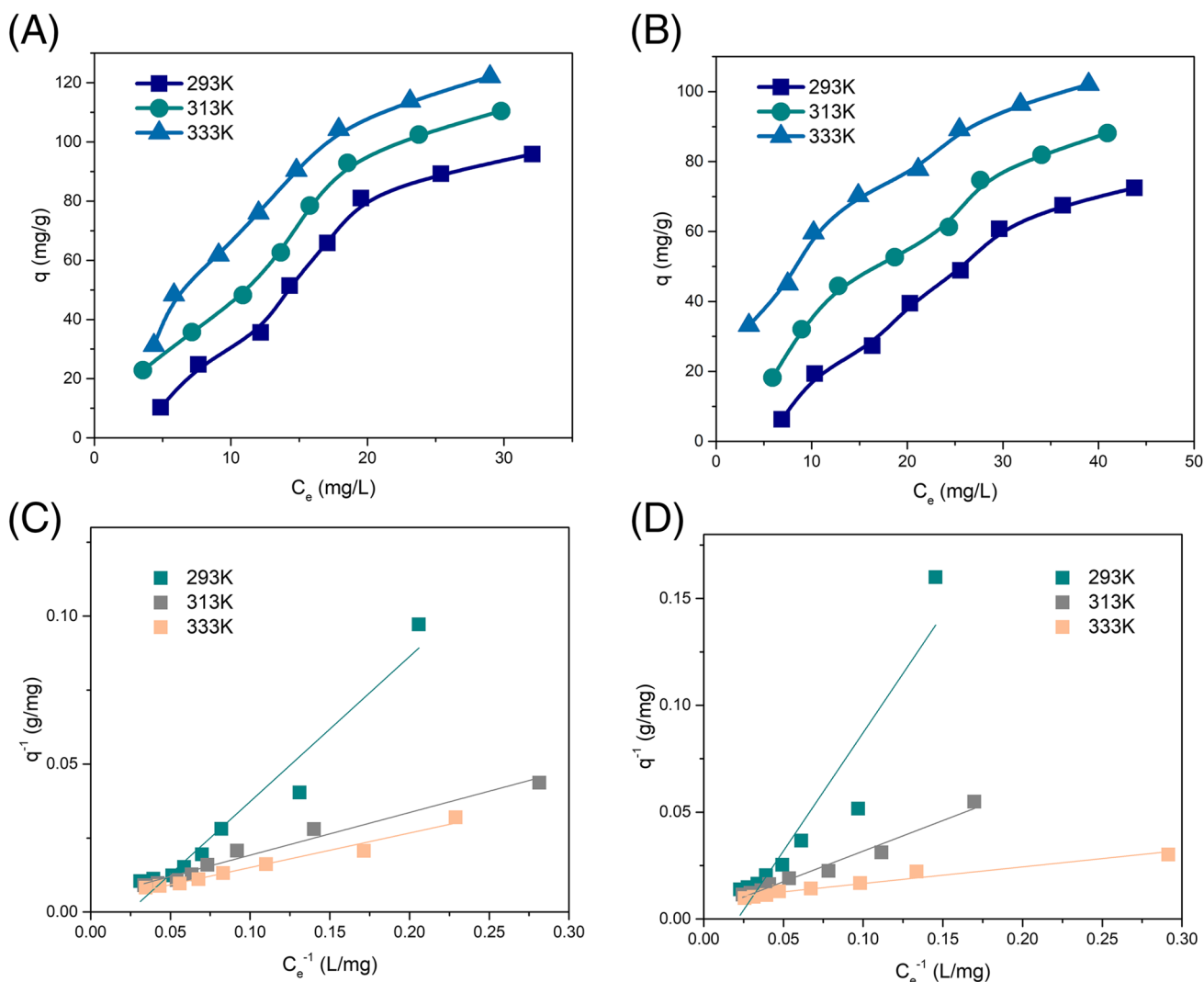
Fig. 7 Isotherm and fitting results of Langmuir of U(VI) (**A**) and Th(IV) (**C**) adsorption on biochar; isotherm and fitting results of Freundlich adsorption isotherms of U(VI) (**B**) and Th(IV) (**D**) adsorption on biochar

Table 1 Langmuir and Freundlich isotherm parameters of U(VI) and Th (IV) adsorption on biochar

Absorbate	T (K)	Langmuir			Freundlich		
		q_{max} (mg/g)	b (L/mg)	R^2	K_f (mg^{1-n}·L^n/g)	n	R^2
U (VI)	293	1527.02	0.0009	0.9888	1.35	1.02	0.9878
	313	399.85	0.0049	0.9932	3.18	1.23	0.9941
	333	261.26	0.0109	0.9911	6.31	1.47	0.9975
Th (IV)	293	1158.16	0.0009	0.9884	1.01	1.01	0.9875
	313	364.48	0.0038	0.9956	2.11	1.18	0.9934
	333	260.98	0.0007	0.9975	3.95	1.37	0.9931

The superficial functional groups on the surface and porous and permeable structure mediated the U(VI) and Th(IV) adsorption biochar. Therefore, the U(VI) and Th(IV) adsorption by biochar both fitted well to the Langmuir and Freundlich models.

3.5 Adsorption thermodynamic calculation

The vital thermodynamic parameters such as standard enthalpy (ΔH_0), standard entropy (ΔS_0), and standard Gibbs

Table 2 Values of thermodynamic parameters for the adsorption of U(VI) and Th (IV)on biochar

Absorbate	ΔH (kJ/mol)	ΔS (J·mol^{-1}·K^{-1})	Δ G (kJ/mol)		
			293 K	313 K	333 K
U (VI)	36.28	108.84	−31.89	−34.07	−36.24
Th (IV)	63.42	134.12	−39.30	−41.98	−44.66

free energy (ΔG_0) were also presented to assess the adsorption thermodynamic of the U(VI) and Th(IV) adsorption process (Table 2). These parameters were calculated based on the following equations:

$$K_d = \frac{C_0 - C_e}{C_e} \frac{V}{m} \tag{4}$$

$$\ln K_d = \frac{\Delta S^0}{R} - \frac{\Delta H^0}{RT} \tag{5}$$

$$\Delta G^0 = \Delta H^0 - T\Delta S^0 \tag{6}$$

C_0 (mg/L) is the initial concentration and C_e (mg/L) indicates the equilibration concentration of the U(VI) and Th(IV) in aqueous solution respectively; V (mL) and m (g) are employed as the volume and mass of biochar as the adsorbent; T (K) and R (8.314 J·mol^{-1}·K^{-1}) represent the temperature in Kelvin and the ideal gas constant.

Both the values of standard enthalpy (ΔH^0) of U(VI) and Th(IV) removals were positive (Table 2). These positive standard enthalpy values indicated the endothermicity of the radionuclide removal processes. The positive values of standard entropy (ΔS^0) reflected the increased randomness of the adsorption processes (Donat, 2009). The negative values of standard Gibbs free energy (ΔG^0) confirmed the feasibility and spontaneity of the U(VI) and Th(IV) adsorption on biochar. Furthermore, the absolute value of standard Gibbs free energy (ΔG^0) grew with the ascending temperature. This finding further supported the assertation that U(VI) and Th(IV) adsorption was spontaneous and this temperature favor was also consistent with the isotherm results referred to above. The endothermicity and spontaneity made biochar a promisingly low-cost and easy-to-operate adsorbent for continuously carrying out the aqueous radionuclide removal. The similar spontaneity, endothermic nature, and temperature favor of the U(VI) and Th(IV) adsorption on biochar were also supported by previous studies [38, 39, 74]. These might be imputed to the external energy offered by the enhanced temperature and heat for binding the aqueous contaminant ions on the electropolymerized surface of biochar [2, 56, 75]. In addition, the thermodynamic parameters provided evidence to verify that both physical and chemical adsorption occurred in U(VI) and Th(IV) removal processes

by biochar. Usually, physical adsorption takes van der Waals force as the adsorptive attraction and the ΔG^0 of physical adsorption was in the range of − 20 to 0 and kJ/mol. As for the chemical adsorption, chemical bonds played a major role and ΔG^0 fell in the interval of − 400 to − 80 kJ/mol. In this regard, the ΔG^0 of U(VI) and Th(IV) removal processes all fell in the range of − 50 to − 30 kJ/mol, which implied that these adsorption processes combined the physical and chemical adsorptions.

4 Conclusion

This work investigated the U(VI) and Th(IV) removals in an aqueous solution to better understand the mechanism of biochar as the radionuclide adsorbent. Results exhibited fitness to the pseudo-second-order and various pH effects on U(VI) and Th(IV) adsorption capacities of biochar. Comparably, only U(VI) rather than Th(IV) adsorption was influenced by interfering ions. Data also fitted the Langmuir and Freundlich model well and revealed the adsorption natures such as endothermicity, increasing randomness, feasibility, spontaneity, and temperature favor of U(VI) and Th(IV) removal. This study provides systematic evidence to prove the potential of biochar as a green sorbent for radioactive contaminants.

References

1. Alessi DS, Lezama-Pacheco JS, Janot N, Suvorova EI, Cerrato JM, Giammar DE, Davis JA, Fox PM, Williams KH, Long PE, Handley KM, Bernier-Latmani R, Bargar JR (2014) Speciation and reactivity of uranium products formed during in situ bioremediation in a shallow alluvial aquifer. Environ Sci Technol 48:12842–12850
2. Sun J, Lian F, Liu Z, Zhu L, Song Z (2014) Biochars derived from various crop straws: characterization and Cd(II) removal potential. Ecotoxicol Environ Saf 106:226–231
3. Sharma P, Tomar R (2011) Sorption behaviour of nanocrystalline MOR type zeolite for Th(IV) and Eu(III) removal from aqueous waste by batch treatment. J Colloid Interface Sci 362:144–156
4. Liatsou I, Christodoulou E, Pashalidis I (2018) Thorium adsorption by oxidized biochar fibres derived from Luffa cylindrica sponges. J Radioanal Nuclear Chem 317:1065–1070
5. Sun Y, Yang S, Sheng G, Guo Z, Tan X, Xu J, Wang X (2011) Comparison of U(VI) removal from contaminated groundwater by nanoporous alumina and non-nanoporous alumina. Separat Purif Technol 83:196–203
6. Sun Y, Wang Q, Chen C, Tan X, Wang X (2012) Interaction between Eu(III) and graphene oxide nanosheets investigated by batch and extended X-ray absorption fine structure spectroscopy and by modeling techniques. Environ Sci Technol 46:6020–6027

7. Li J, Guo Z, Zhang S, Wang X (2011) Enrich and seal radionuclides in magnetic agarose microspheres. Chem Eng J 172:892–897

8. Shi W-Q, Zhao Y-L, Chai Z-F (2012) Nuclear and radiochemistry in China: present status and future perspectives. Radiochim Acta 100:529–539

9. Pang H, Diao Z, Wang X, Ma Y, Yu S, Zhu H, Chen Z, Hu B, Chen J, Wang X (2019) Adsorptive and reductive removal of U(VI) by Dictyophora indusiate-derived biochar supported sulfide NZVI from wastewater. Chem Eng J 366:368–377

10. Hu Q, Zhu Y, Hu B, Lu S, Sheng G (2018) Mechanistic insights into sequestration of U(VI) toward magnetic biochar: batch, XPS and EXAFS techniques. J Environ Sci (China) 70:217–225

11. Dong L, Chang K, Wang L, Linghu W, Zhao D, Asiri AM, Alamry KA, Alsaedi A, Hayat T, Li X, Wu X (2017) Application of biochar derived from rice straw for the removal of Th(IV) from aqueous solution. Separat Sci Technol 53:1511–1521

12. Dong L, Yang J, Mou Y, Sheng G, Wang L, Linghu W, Asiri AM, Alamry KA (2017) Effect of various environmental factors on the adsorption of U(VI) onto biochar derived from rice straw. J Radioanal Nuclear Chem 314:377–386

13. Chandramouleeswaran S, Ramkumar J, Sudarsan V, Reddy AV (2011) Boroaluminosilicate glasses: novel sorbents for separation of Th and U. J Hazard Mater 198:159–164

14. Jin J, Li S, Peng X, Liu W, Zhang C, Yang Y, Han L, Du Z, Sun K, Wang X (2018) HNO3 modified biochars for uranium (VI) removal from aqueous solution. Bioresour Technol 256:247–253

15. Alam MS, Gorman-Lewis D, Chen N, Safari S, Baek K, Konhauser KO, Alessi DS (2018) Mechanisms of the removal of U(VI) from aqueous solution using biochar: a combined spectroscopic and modeling approach. Environ Sci Technol 52:13057–13067

16. Salah, Gaber, Kandil (2019) The removal of uranium and thorium from their aqueous solutions by 8-hydroxyquinoline immobilized bentonite. Minerals 9:626

17. Ye T, Huang B, Wang Y, Zhou L, Liu Z (2020) Rapid removal of uranium(VI) using functionalized luffa rattan biochar from aqueous solution. Colloid Surf A Physicochem Eng Aspect 606:125480

18. Wang J, Ma R, Li L, Gu P, Wang X (2019) Chitosan modified molybdenum disulfide composites as adsorbents for the simultaneous removal of U(VI), Eu(III), and Cr(VI) from aqueous solutions. Cellulose 27:1635–1648

19. Inyang MI, Gao B, Yao Y, Xue Y, Zimmerman A, Mosa A, Pullammanappallil P, Ok YS, Cao X (2015) A review of biochar as a low-cost adsorbent for aqueous heavy metal removal. Crit Rev Environ Sci Technol 46:406–433

20. Mohan D, Sarswat A, Ok YS, Pittman CU Jr (2014) Organic and inorganic contaminants removal from water with biochar, a renewable, low cost and sustainable adsorbent–a critical review. Bioresour Technol 160:191–202

21. Chen W, Meng J, Han X, Lan Y, Zhang W (2019) Past, present, and future of biochar. Biochar 1:75–87

22. Lehmann J, Gaunt J, Rondon M (2006) Bio-char sequestration in terrestrial ecosystems – a review. Mitigat Adapt Strateg Gl Chang 11:403–427

23. Lehmann J, Rillig MC, Thies J, Masiello CA, Hockaday WC, Crowley D (2011) Biochar effects on soil biota – a review. Soil Biol Biochem 43:1812–1836

24. Cao Q, Huang Z, Liu S, Wu Y (2019) Potential of Punica granatum biochar to adsorb Cu(II) in soil. Sci Rep 9:11116

25. Hu B, Ai Y, Jin J, Hayat T, Alsaedi A, Zhuang L, Wang X (2020) Efficient elimination of organic and inorganic pollutants by biochar and biochar-based materials. Biochar 2:47–64

26. Igalavithana AD, Mandal S, Niazi NK, Vithanage M, Parikh SJ, Mukome FND, Rizwan M, Oleszczuk P, Al-Wabel M, Bolan N, Tsang DCW, Kim K-H, Ok YS (2018) Advances and future directions of biochar characterization methods and applications. Crit Rev Environ Sci Technol 47:2275–2330

27. Kwak JH, Islam MS, Wang S, Messele SA, Naeth MA, El-Din MG, Chang SX (2019) Biochar properties and lead(II) adsorption capacity depend on feedstock type, pyrolysis temperature, and steam activation. Chemosphere 231:393–404

28. Lu H, Zhang W, Yang Y, Huang X, Wang S, Qiu R (2012) Relative distribution of Pb2+ sorption mechanisms by sludge-derived biochar. Water Res 46:854–862

29. Regmi P, Garcia Moscoso JL, Kumar S, Cao X, Mao J, Schafran G (2012) Removal of copper and cadmium from aqueous solution using switchgrass biochar produced via hydrothermal carbonization process. J Environ Manage 109:61–69

30. Liu N, Zhang Y, Xu C, Liu P, Lv J, Liu Y, Wang Q (2020) Removal mechanisms of aqueous Cr(VI) using apple wood biochar: a spectroscopic study. J Hazard Mater 384:121371

31. Cao X, Harris W (2010) Properties of dairy-manure-derived biochar pertinent to its potential use in remediation. Bioresour Technol 101:5222–5228

32. Dong X, Ma LQ, Li Y (2011) Characteristics and mechanisms of hexavalent chromium removal by biochar from sugar beet tailing. J Hazard Mater 190:909–915

33. Wang S, Gao B, Zimmerman AR, Li Y, Ma L, Harris WG, Migliaccio KW (2015) Removal of arsenic by magnetic biochar prepared from pinewood and natural hematite. Bioresour Technol 175:391–395

34. Ahmad M, Rajapaksha AU, Lim JE, Zhang M, Bolan N, Mohan D, Vithanage M, Lee SS, Ok YS (2014) Biochar as a sorbent for contaminant management in soil and water: a review. Chemosphere 99:19–33

35. Cao X, Ma L, Liang Y, Gao B, Harris W (2011) Simultaneous immobilization of lead and atrazine in contaminated soils using dairy-manure biochar. Environ Sci Technol 45:4884–4889

36. Ahmad M, Lee SS, Dou X, Mohan D, Sung JK, Yang JE, Ok YS (2012) Effects of pyrolysis temperature on soybean stover- and peanut shell-derived biochar properties and TCE adsorption in water. Bioresour Technol 118:536–544

37. Li N, Yin M, Tsang DCW, Yang S, Liu J, Li X, Song G, Wang J (2019) Mechanisms of U(VI) removal by biochar derived from Ficus microcarpa aerial root: a comparison between raw and modified biochar. Sci Total Environ 697: 134115

38. Wang B, Li Y, Zheng J, Hu Y, Wang X, Hu B (2020) Efficient removal of U(VI) from aqueous solutions using the magnetic biochar derived from the biomass of a bloom-forming cyanobacterium (Microcystis aeruginosa). Chemosphere 254: 126898

39. Wang X, Feng J, Cai Y, Fang M, Kong M, Alsaedi A, Hayat T, Tan X (2020) Porous biochar modified with polyethyleneimine (PEI) for effective enrichment of U(VI) in aqueous solution. Sci Total Environ 708: 134575

40. Zhao QZ, Wang YF, Xu ZH, Yu ZS (2021) Removal mechanisms of Cd(II) and Pb(II) from aqueous solutions using straw biochar: batch study, Raman and X-ray photoelectron spectroscopy techniques. Desalin Water Treat 220:199–210

41. Hu B, Wang H, Liu R, Qiu M (2021) Highly efficient U(VI) capture by amidoxime/carbon nitride composites: evidence of EXAFS and modeling. Chemosphere 274: 129743

42. Humelnicu D, Bulgariu L, Macoveanu M (2010) On the retention of uranyl and thorium ions from radioactive solution on peat moss. J Hazard Mater 174:782–787

43. Lehmann J, Bossio DA, Kogel-Knabner I, Rillig MC (2020) The concept and future prospects of soil health. Nat Rev Earth Environ 1:544–553

44. Antón-Herrero R, García-Delgado C, Alonso-Izquierdo M, García-Rodríguez G, Cuevas J, Eymar E (2018) Comparative adsorption of tetracyclines on biochars and stevensite: looking for the most effective adsorbent. Appl Clay Sci 160:162–172

45. Mendez A, Tarquis AM, Saa-Requejo A, Guerrero F, Gasco G (2013) Influence of pyrolysis temperature on composted sewage sludge biochar priming effect in a loamy soil. Chemosphere 93:668–676

46. Chi T, Zuo J, Liu F (2017) Performance and mechanism for cadmium and lead adsorption from water and soil by corn straw biochar. Front Environ Sci Eng 11:15

47. Chia CH, Gong B, Joseph SD, Marjo CE, Munroe P, Rich AM (2012) Imaging of mineral-enriched biochar by FTIR, Raman and SEM–EDX. Vibrat Spectrosc 62:248–257

48. Lyu H, Tang J, Huang Y, Gai L, Zeng EY, Liber K, Gong Y (2017) Removal of hexavalent chromium from aqueous solutions by a novel biochar supported nanoscale iron sulfide composite. Chem Eng J 322:516–524

49. Genovese M, Jiang J, Lian K, Holm N (2015) High capacitive performance of exfoliated biochar nanosheets from biomass waste corn cob. J Mater Chem A 3:2903–2913

50. Wang XL, Xing BS (2007) Importance of structural makeup of biopolymers for organic contaminant sorption. Environ Sci Technol 41:3559–3565

51. Young KD, Leboeuf EJ (2000) Glass transition behavior in a peat humic acid and an aquatic fulvic acid. Environ Sci Technol 34:4549–4553

52. Zhang W, Mao S, Chen H, Huang L, Qiu R (2013) Pb(II) and Cr(VI) sorption by biochars pyrolyzed from the municipal wastewater sludge under different heating conditions. Bioresour Technol 147:545–552

53. Aytas S, Yurtlu M, Donat R (2009) Adsorption characteristic of U(VI) ion onto thermally activated bentonite. J Hazard Mater 172:667–674

54. Ali O, Osman HH, Sayed SA, Shalabi MEH (2013) The removal of uranium and thorium from their aqueous solutions via glauconite. Desalin Water Treat 53:760–767

55. Hu H, Zhang X, Wang T, Sun L, Wu H, Chen X (2018) Bamboo (Acidosasa longiligula) shoot shell biochar: its potential application to isolation of uranium(VI) from aqueous solution. J Radioanal Nucl Chem 316:349–362

56. Liu Z, Zhang FS (2009) Removal of lead from water using biochars prepared from hydrothermal liquefaction of biomass. J Hazard Mater 167:933–939

57. Sheng G, Dong H, Li Y (2012) Characterization of diatomite and its application for the retention of radiocobalt: role of environmental parameters. J Environ Radioact 113:108–115

58. Sheng G, Dong H, Shen R, Li Y (2013) Microscopic insights into the temperature-dependent adsorption of Eu(III) onto titanate nanotubes studied by FTIR, XPS, XAFS and batch technique. Chem Eng J 217:486–494

59. Sheng G, Yang Q, Peng F, Li H, Gao X, Huang Y (2014) Determination of colloidal pyrolusite, Eu(III) and humic substance interaction: a combined batch and EXAFS approach. Chem Eng J 245:10–16

60. Sheng GD, Yang ST, Li YM, Gao X, Huang YY, Hu J, Wang XK (2014) Retention mechanisms and microstructure of Eu(III) on manganese dioxide studied by batch and high resolution EXAFS technique. Radiochim Acta 102:155–167

61. Zhao G, Ren X, Gao X, Tan X, Li J, Chen C, Huang Y, Wang X (2011) Removal of Pb(II) ions from aqueous

62. Dai L, Li L, Zhu W, Ma H, Huang H, Lu Q, Yang M, Ran Y (2020) Post-engineering of biochar via thermal air treatment for highly efficient promotion of uranium(VI) adsorption. Bioresour Technol 298: 122576

63. Xu Z, Xing Y, Ren A, Ma D, Li Y, Hu S (2020) Study on adsorption properties of water hyacinth-derived biochar for uranium (VI). J Radioanal Nucl Chem 324:1317–1327

64. Worthen AJ, Lapitsky Y (2011) Stabilization of bioderived surfactant/polyelectrolyte complexes through surfactant conjugation to the biopolymer. Colloid Polym Sci 289:1589–1596

65. Dai S, Wang N, Qi C, Wang X, Ma Y, Yang L, Liu X, Huang Q, Nie C, Hu B, Wang X (2019) Preparation of core-shell structure Fe3O4@C@MnO2 nanoparticles for efficient elimination of U(VI) and Eu(III) ions. Sci Total Environ 685:986–996

66. Qiu M, Liu Z, Wang S, Hu B (2021) The photocatalytic reduction of U(VI) into U(IV) by ZIF-8/g-C3N4 composites at visible light. Environ Res 196: 110349

67. Kusrini E, Wicaksono W, Gunawan C, Daud NZA, Usman A (2018) Kinetics, mechanism, and thermodynamics of lanthanum adsorption on pectin extracted from durian rind. J Environ Chem Eng 6:6580–6588

68. Chang K, Sun Y, Ye F, Li X, Sheng G, Zhao D, Linghu W, Li H, Liu J (2017) Macroscopic and molecular study of the sorption and co-sorption of graphene oxide and Eu(III) onto layered double hydroxides. Chem Eng J 325:665–671

69. Hu B, Hu Q, Chen C, Sun Y, Xu D, Sheng G (2017) New insights into Th(IV) speciation on sepiolite: evidence for EXAFS and modeling investigation. Chem Eng J 322:66–72

70. Hu B, Ye F, Ren X, Zhao D, Sheng G, Li H, Ma J, Wang X, Huang Y (2016) X-ray absorption fine structure study of enhanced sequestration of U(vi) and Se(iv) by montmorillonite decorated with zero-valent iron nanoparticles. Environ Sci Nano 3:1460–1472

71. Hu XJ, Wang JS, Liu YG, Li X, Zeng GM, Bao ZL, Zeng XX, Chen AW, Long F (2011) Adsorption of chromium (VI) by ethylenediamine-modified cross-linked magnetic chitosan resin: isotherms, kinetics and thermodynamics. J Hazard Mater 185:306–314

72. Kim WK, Shim T, Kim YS, Hyun S, Ryu C, Park YK, Jung J (2013) Characterization of cadmium removal from aqueous solution by biochar produced from a giant Miscanthus at different pyrolytic temperatures. Bioresour Technol 138:266–270

73. Tan X, Liu Y, Zeng G, Wang X, Hu X, Gu Y, Yang Z (2015) Application of biochar for the removal of pollutants from aqueous solutions. Chemosphere 125:70–85

74. Li M, Liu H, Chen T, Dong C, Sun Y (2019) Synthesis of magnetic biochar composites for enhanced uranium(VI) adsorption. Sci Total Environ 651:1020–1028

75. Parshetti GK, Chowdhury S, Balasubramanian R (2014) Hydrothermal conversion of urban food waste to chars for removal of textile dyes from contaminated waters. Bioresour Technol 161:310–319

Publisher's note Springer Nature remains neutral with regard to jurisdictional claims in published maps and institutional affiliations.